Thermoelectric properties of SnSe and $SnSe_2$ single crystals

Abhinna Rajbanshi,[1] Daniel Duong,[1] Eklavya Thareja,[2] Williams A. Shelton,[2] and Rongying Jin[1,*]

[1]*SmartState Center for Experimental Nanoscale Physics, Department of Physics and Astronomy, University of South Carolina, Columbia, South Carolina 29208, USA*

[2]*Department of Physics and Astronomy, Louisiana State University, Baton Rouge, Louisiana 70803, USA*

(Received 27 October 2023; accepted 1 February 2024; published 20 February 2024)

Thermoelectric materials can serve for conversion between thermal and electrical energy. In the search for thermoelectric materials, layered SnSe and $SnSe_2$ are promising candidates. We have successfully synthesized SnSe and $SnSe_2$ single crystals by the modified Bridgman method and studied their thermoelectric properties: thermopower (S), thermal conductivity (κ), and electrical conductivity (σ) in the temperature range between 2 and 400 K, which are absent in the literature. The kink observed in the thermopower corresponds to the metallic-nonmetallic crossover temperature for both SnSe and $SnSe_2$, reflecting their inherent electronic nature. Compared with $SnSe_2$, >100 K, we find that SnSe exhibits higher electrical conductivity, higher thermopower, and lower thermal conductivity, thus resulting in the higher figure of merit. Hall effect measurements reveal that the Hall mobility in SnSe is an order higher than that in $SnSe_2$, advancing its thermoelectric performance. These experimental results are supported by first-principles calculations, which indicate that the inequivalent Sn-Se bonding lengths help improve the figure of merit of SnSe.

DOI: 10.1103/PhysRevMaterials.8.023601

I. INTRODUCTION

The energy needs in the world increase day by day, and most energy produced comes from nonrenewable energy resources such as coal, petroleum, natural gas, and nuclear energy [1]. The consumption of these energy resources causes global warming. Thermoelectric materials, which allow the direct energy conversion between heat and electricity, can alleviate these issues [1,2]. The figure of merit $ZT = \frac{S^2\sigma T}{\kappa}$ determines the performance of the thermoelectric materials [3,4], where S is the thermopower, σ is the electrical conductivity, T is the absolute temperature, and κ is the thermal conductivity. Since S, σ, and κ are interdependent, it is not trivial to enhance the figure of merit by solely optimizing one parameter in a bulk material. In the search for high-performance thermoelectrics, materials with layered crystal structures are extremely attractive, as both the electrical and thermal conductivities can be disentangled. The bonding heterogeneity between intralayer and interlayer provides a great opportunity to generate good electrical conductivity within layers but low thermal conductivity due to increased electron-phonon scattering [5,6]. Further improvement can be achieved via introducing chemical doping and nanostructure, etc. [3,4,7–15].

Among layered materials, SnSe and $SnSe_2$ are promising candidates due to their low thermal conductivity and high thermopower resulting from their unique crystal structures [16,17]. Both SnSe and $SnSe_2$ have anisotropic electrical and thermal properties between intralayers and interlayers [18,19]. However, presented in the literature are varying values for the thermal conductivity due to possible sample oxidation, nonstoichiometry, and other impurities [19]. For example, the thermal conductivity of SnSe was reported to vary between 0.7 and 2.32 $W\,K^{-1}\,m^{-1}$ at room temperature [16,20–22]. The low thermal conductivity in Ref. [16] was attributed to the presence of $SnSe_2$ in the SnSe crystal matrix, which not only produces Sn vacancies but also forms microdomains. However, the $SnSe_2$ inclusion cannot solely account for the ultralow thermal conductivity reported in Ref. [16], as commented in Ref. [23]. Therefore, it is important to understand the crystal structures and thermoelectric properties of SnSe and $SnSe_2$ in their pure forms. Although there are a few studies of SnSe and $SnSe_2$ at high temperatures (300 K $\leqslant T \leqslant$ 900 K) [16–19,21,24,25], low-temperature ($T \leqslant$ 300 K) thermoelectric properties of both SnSe and $SnSe_2$ single crystals have not been investigated thoroughly.

In this paper, we report on the growth of SnSe and $SnSe_2$ single crystals by the modified Bridgman method and the investigation of their thermoelectric properties. Overall, SnSe exhibits better thermoelectric properties than that of $SnSe_2$ between 2 and 400 K, which is absent in the literature. To help understand the underlying physics, the Hall effect, specific heat, and electron and phonon band structures were investigated. The higher Hall mobility of SnSe advances its figure of merit over $SnSe_2$. This can be explained by the unique crystal structure of SnSe, which provides a hopping path for electrical conduction but damps the thermal conductivity due to inequivalent Sn-Se bonding lengths. The comparative study between SnSe and $SnSe_2$ offers important information for understanding the underlying charge and heat transport.

II. EXPERIMENTAL AND COMPUTATIONAL DETAILS

Single crystals of SnSe and $SnSe_2$ were grown using the modified Bridgman method, as described in Ref. [26].

*rjin@mailbox.sc.edu

The elemental Sn shots (99.99%, Alfa Aesar) and Se powder (99.999%, Alfa Aesar) with molar ratios of Sn : Se = 1:1 and 1:2 for SnSe and $SnSe_2$, respectively, were sealed in evacuated quartz tubes. The tubes were slowly heated (60 °C/h) up to 900°C and held at this temperature for 24 h. The samples were then slowly cooled (2 °C/h) to 200 °C and finally cooled to room temperature by turning off the furnace. The crystal structures of both SnSe and $SnSe_2$ were determined by x-ray diffraction (XRD), Rigaku Ultima IV, using Cu $K\alpha$ radiation ($\lambda = 1.5406$ Å). The stoichiometry and elemental distribution of SnSe and $SnSe_2$ crystals were analyzed by energy-dispersive x-ray spectroscopy (EDX). The thermal conductivity and thermopower were measured using the thermal transport option mode of a Physical Properties Measurement System (PPMS DynaCool) between 2 and 400 K, while the electrical conductivity was measured using the resistivity option of the PPMS. Hall measurements were carried out in the resistivity option of the PPMS at various temperatures using the four-probe method with magnetic field up to ±14 T. Heat capacity measurements were carried out on a 10.5 mg sample of SnSe and a 16.8 mg sample of $SnSe_2$ in the PPMS between 2 and 400 K.

The structural, vibrational, and electronic properties of SnSe and $SnSe_2$ were calculated using VASP [27–30]. The projector augmented-wave pseudopotentials [31] with the Perdew-Burke-Ernzerhof exchange-correlation functional [32] were employed for Sn ($4d^{10}$, $5s^2$, $5p^2$) and Se ($4s^2$, $4p^4$). In addition, van der Waals (vdW) interactions were treated using the semiempirical density function theory (DFT)-D2 method of Grimme [33]. Other methods including semiempirical DFT-D3 [34,35], the Tkatchenko-Scheffler method with iterative Hirschfeld partitioning [36,37], the nonlocal-vdW functionals optB88 [38] and optB86b [39], as well as both meta-GGA SCAN [40] and r^{2}SCAN [41] DFT combined with rVV10 were investigated.

III. RESULTS AND DISCUSSIONS

Figures 1(a) and 1(b) display the XRD result obtained from the flat planes of SnSe and $SnSe_2$ single crystals (red curves), respectively. Compared with that in the Inorganic Crystal Structure Database (black curves), the XRD patterns for both SnSe and $SnSe_2$ confirm that they exhibit pure phases. SnSe forms the orthorhombic crystal structure (*pnma*), as shown in Fig. 1(c), with the lattice constants $a = 11.489$ Å, $b = 4.1527$ Å, and $c = 4.4456$ Å. The crystal structure and lattice parameters are consistent with the previous report [42]. $SnSe_2$ crystalizes in the hexagonal structure, as shown in Fig. 1(d), with the lattice parameters of $SnSe_2$ $a = b = 3.8128$ Å and $c = 6.1373$ Å, which are consistent with that in Ref. [18]. EDX measurements show that the ratio of Sn and Se is 1:1 for SnSe and 1:2 for $SnSe_2$, i.e., both compounds are stochiometric.

Figures 2(a) and 2(b) show the temperature dependence of the in-plane electrical conductivities of SnSe (σ_b and σ_c) and $SnSe_2$ (σ_{ab}) single crystals, respectively. Upon increasing the temperature, both σ_b and σ_c of SnSe [Fig. 2(a)] initially rise until reaching 60.74 Ω^{-1} cm^{-1} for σ_b at $T_x = 78$ K and 63.50 Ω^{-1} cm^{-1} for σ_c at $T_x = 68$ K for σ_c, above which they decrease. The values of σ_b (300 K) and σ_c (300 K) are

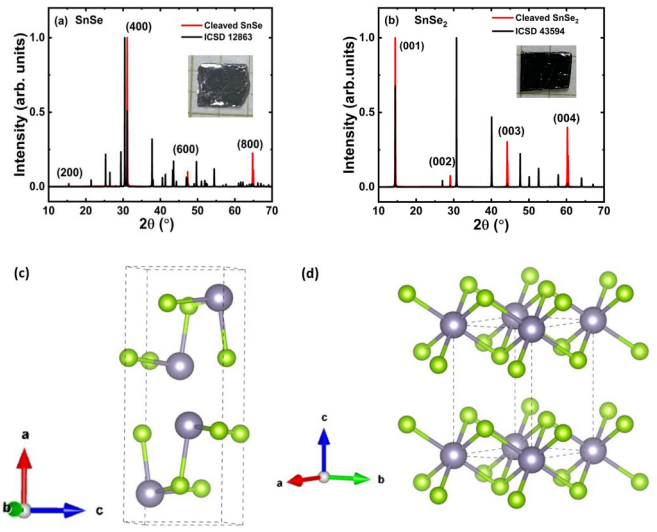

FIG. 1. X-ray diffraction (XRD) patterns for (a) SnSe and (b) $SnSe_2$ single crystals. Red represents data from our single crystals, and black denotes that from the Inorganic Crystal Structure Database (ICSD). Crystal structures of (c) SnSe and (d) $SnSe_2$. Gray balls represent Sn atoms and green balls Se atoms.

18.60 and 17.24 Ω^{-1} cm^{-1}, respectively. These values are much higher than that for $SnSe_2$ with the maximum ~4.5 Ω^{-1} cm^{-1} at $T_x = 105$ K and ~2.5 Ω^{-1} cm^{-1} at 300 K [Fig. 2(b)]. The room-temperature electrical conductivities for

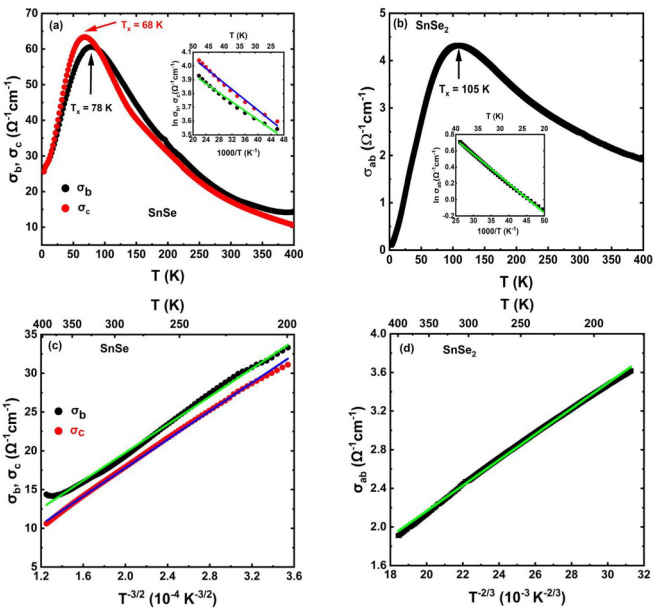

FIG. 2. (a) Temperature dependence of the in-plane electrical conductivity (σ_b and σ_c) of a SnSe single crystal. The inset represents the plot of lnσ_b and lnσ_c vs 1000/T in the temperature range between 20 and 45 K. (b) Temperature dependence of the in-plane conductivity (σ_{ab}) of $SnSe_2$, and the inset plots lnσ_{ab} vs 1000/T in the temperature range between 20 and 40 K. (c) σ_b and σ_c vs $T^{-3/2}$ plot for SnSe between 150 and 400 K with the linear fitting lines (green and blue). (d) σ_{ab} vs $T^{-2/3}$ for $SnSe_2$ in the temperature range between 180 and 400 K (black) with the linear fitting line (green).

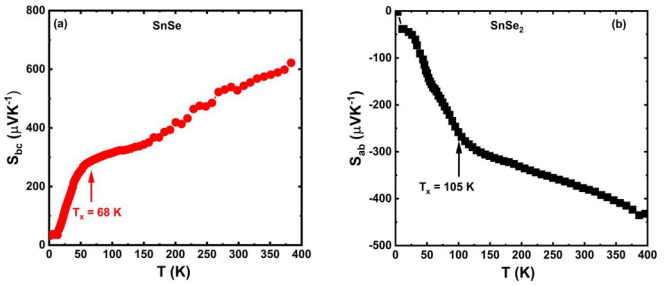

FIG. 3. Temperature dependence of the thermopower of (a) SnSe and (b) $SnSe_2$.

SnSe are comparable with that reported in Ref. [16]. This is surprising, as Ref. [16] mentions the inclusion of $SnSe_2$ and Sn vacancies in SnSe. Such an imperfection should result in lower electrical conductivity due to poorer electrical conduction in $SnSe_2$ [Fig. 2(b)] and Sn vacancies. Nevertheless, in the nonmetallic region ($T < T_x$), the electrical conductivity is expected to follow $\sigma = \sigma_0 \exp[-\frac{E_g}{k_B T}]$ for describing thermally activated electrical conduction with the activation energy E_g, where σ_0 is a constant and k_B is the Boltzmann constant. From the plot of $\ln\sigma_b$ and $\ln\sigma_c$ vs $1000/T$, as shown in the inset of Fig. 2(a), the suitable fitting region is 20–45 K, which gives $E_g \sim 1.35 \pm 0.01$ meV from σ_b and 1.56 ± 0.01 meV from σ_c. These values are much smaller than that obtained from the optical reflectivity [43]. On the other hand, from the plot of $\ln\sigma_{ab}$ vs $1000/T$ in the temperature range between 20 and 40 K shown in the inset of Fig. 2(b), the activation energy of $SnSe_2$ is found to be $E_g \sim 3.10 \pm 0.02$ meV. Again, this is clearly underestimated, as it is much smaller than the energy gap from either experiment [43,44] or calculations [45]. The low E_g values for both SnSe and $SnSe_2$ suggest there are additional conduction channels that slow down the decrease of the electrical conduction at low temperatures, which will be discussed later. In the metallic region ($T > T_x$), we find that both σ_b and σ_c for SnSe follow $T^{-3/2}$ dependence in the temperature range between 200 and 400 K, as shown in Fig. 2(c). For $SnSe_2$, σ_{ab} exhibits a $T^{-2/3}$ behavior in the temperature region between 180 and 400 K, as illustrated in Fig. 2(d). The origin of such temperature dependence is discussed later.

Figures 3(a) and 3(b) present the temperature dependence of the in-plane thermopower for SnSe (S_{bc}) and $SnSe_2$ (S_{ab}) single crystals in the temperature range between 2 and 400 K, respectively. Note that S_{bc} for SnSe increases with increasing temperature in the whole temperature range ($2\ \text{K} \leqslant T \leqslant 400\ \text{K}$) with $531\ \mu\text{V K}^{-1}$ at 300 K, consistent with previous work [16,44,45] but different in both temperature dependence and magnitude from that shown in Ref. [26].

The positive sign of S_{bc} suggests that dominant charge carriers are holes in SnSe. On the other hand, S_{ab} for $SnSe_2$ is negative with $-378\ \mu\text{V K}^{-1}$ at 300 K, comparable with the reported value [17]. The negative S_{ab} indicates that most charge carriers in $SnSe_2$ are electrons. Interestingly, the thermopower for both SnSe and $SnSe_2$ reveals a slope change at T_x, the crossover temperature from metallic behavior at high temperatures to the nonmetallic character at low temperatures. This indicates the interconnection between the thermopower and electrical conductivity. The slope at $T < T_x$ is much larger than that at $T > T_x$ in both materials, likely due to the change of the electronic structure. For the thermopower, the most relevant quantity is the change of the density of states (DOS) with respect to the energy at the Fermi level $\frac{dN(E)}{dE}$ [11,46]. As will be discussed later, the electronic structures of SnSe and $SnSe_2$ reflect the large $\frac{dN(E)}{dE}$.

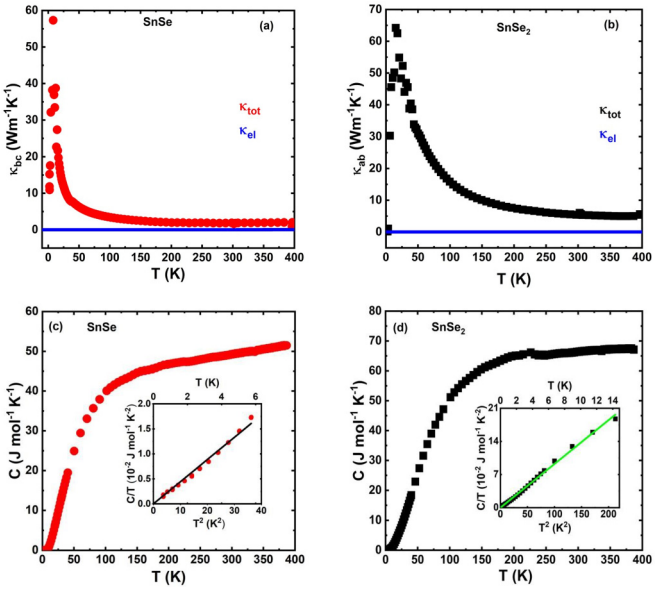

FIG. 4. (a) Temperature dependence of thermal conductivity (κ_{bc}) of a SnSe single crystal (red). The blue line represents the electronic κ_{el}. (b) Temperature dependence of thermal conductivity (κ_{ab}) of a $SnSe_2$ single crystal. The blue line represents the electronic κ_{el}. (c) Temperature dependence of specific heat (C) of a SnSe single crystal. Inset: C/T vs T^2 and the fitted result (solid line). (d) Temperature dependence of the specific heat of a $SnSe_2$ single crystal. Inset: C/T vs T^2 and the fitted result.

Figures 4(a) and 4(b) show the temperature dependence of the thermal conductivity of SnSe (κ_{bc}) and $SnSe_2$ (κ_{ab}) single crystals, respectively. The total thermal conductivity for both SnSe and $SnSe_2$ single crystals exhibits a sharp peak ~8 and 15 K, respectively. Above the peak, the thermal conductivity decreases with T^{-1} for both SnSe and $SnSe_2$, which is the characteristic of Umklapp scattering [47]. The lattice thermal conductivity can be obtained by subtracting the electronic thermal conductivity from the total thermal conductivity, i.e., $\kappa_{\text{lat}} = \kappa_{\text{tot}} - \kappa_{\text{el}}$, where κ_{el} is calculated using the Wiedemann-Franz law $\kappa_{\text{el}} = L\sigma T$. Here, L is the Lorenz number. For both SnSe and $SnSe_2$, $\kappa_{\text{el}} \ll \kappa_{\text{tot}}$. Thus, the lattice contribution $\kappa_{\text{lat}} \approx \kappa_{\text{tot}}$. At 300 K, the thermal conductivities of SnSe and $SnSe_2$ single crystals are found to be ~1.90 and $5.40\ \text{W K}^{-1}\ \text{m}^{-1}$, respectively. Compared with the calculated result ($\kappa_{b,\text{lat}} \sim 0.75\ \text{W K}^{-1}\ \text{m}^{-1}$) shown in Ref. [16], our κ_{bc} for SnSe is ~3 times higher; a similar experimental result was also reported in Ref. [22]. This is surprising because any crystal imperfection can only result in lower thermal conductivity in experiments. On the other hand, our κ_{ab} for $SnSe_2$ is close to the calculated value [17,18,45], reflecting the good quality of our samples. The discrepancy between measurements by us and Ref. [22] and that in Ref. [16] could

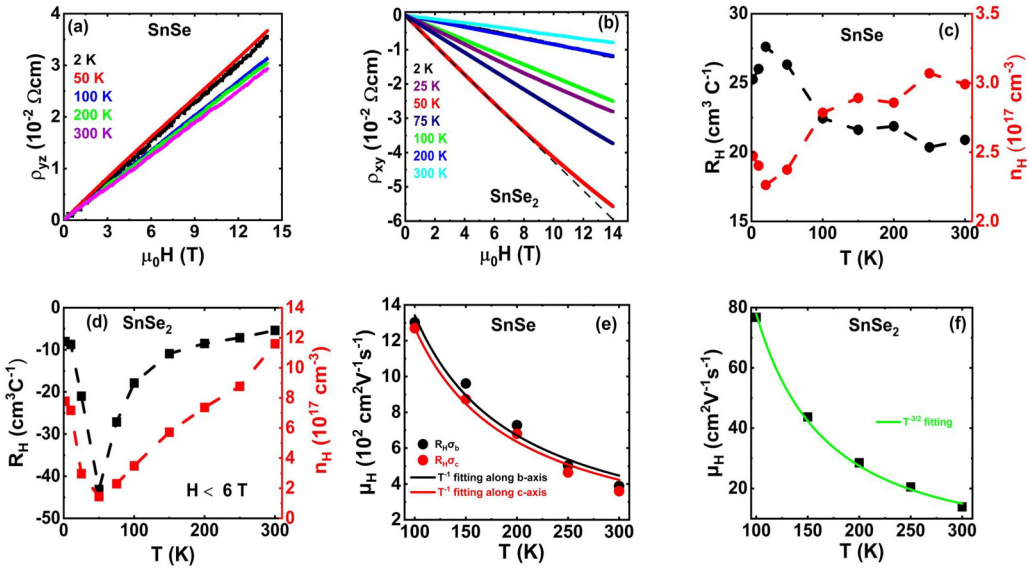

FIG. 5. Magnetic field dependence of the Hall effect of (a) SnSe and (b) $SnSe_2$ single crystals, respectively. Hall coefficient and carrier concentrations of (c) SnSe and (d) $SnSe_2$ as a function of temperature, respectively. (e) Hall mobility (μ_H) vs temperature for SnSe calculated using σ_b (black circles) and σ_c (red circles). The lines are the fits of data with $1/T$ temperature dependence. (f) Hall mobility (μ_H) vs temperature for $SnSe_2$. The line is the fit of data with $T^{-3/2}$ temperature dependence.

be related to that commented in Ref. [23], i.e., the calculated thermal conductivity for SnSe is underestimated.

Although SnSe forms a centrosymmetric structure, the Sn-Se bonding lengths are inequivalent [Fig. 1(c)], giving rise to anharmonicity [16]. $SnSe_2$ lacks such anharmonicity, thus having higher thermal conductivity. To help understand the thermal transport properties, we measure the specific heat of SnSe and $SnSe_2$. Figures 4(c) and 4(d) show the temperature dependence of the specific heat for SnSe and $SnSe_2$ single crystals in the temperature range between 2 and 400 K, respectively. By replotting the low-temperature data to C/T vs T^2, as shown in the insets of Figs. 4(c) and 4(d), we find that C can be described by the Debye T^3 law $C \cong 234Nk_B(\frac{T}{\theta_D})^3$, where N is the number of atoms in the unit cell and θ_D is the Debye temperature. From fitting, θ_D is found to be 206 and 185 K for SnSe and $SnSe_2$, respectively. At $T > \theta_D$, the specific heat of $SnSe_2$ is close to saturation consistent with the classical Dulong-Petit result $C = 3Nk_B$, while it continuously increases for SnSe. With the much different specific heat and thermal conductivity between SnSe and $SnSe_2$, anharmonicity in the formal system may play an important role [16].

To further understand the difference between the two systems, we measure the Hall effect of both SnSe and $SnSe_2$. Figures 5(a) and 5(b) present the magnetic field dependence of the Hall resistivity of SnSe (ρ_{yz}) and $SnSe_2$ (ρ_{xy}) single crystals between 2 and 300 K, respectively. For SnSe, ρ_{yz} increases linearly with the magnetic field at all measured temperatures. We fit the data between 0 and 14 T to $\rho_{yz} = R_H\mu_0 H$ for each temperature, where R_H is the Hall coefficient. Figure 5(c) shows the temperature dependence of R_H of SnSe, which initially increases from 2 to 20 K then falls with increasing temperature. The positive Hall coefficient of SnSe suggests that most charge carriers in SnSe are holes, consistent with the thermopower data. Using the Drude relationship for the single band case with $R_H = \frac{1}{n_H e}$, the carrier concentration (n_H) can be estimated. The carrier concentration of SnSe is found to be 3×10^{17} cm^{-3} at room temperature, which slowly decreases with decreasing temperature until 20 K. For $SnSe_2$, ρ_{xy} depends on H linearly at most temperatures measured, except that ~50 K. As demonstrated in Fig. 5(b), ρ_{xy} (50 K) deviates from the linear behavior >6 T. The development of nonlinearity suggests that the system either involves more than one type of carrier or field-induced electronic structure change. For estimating R_H, we fit all data <6 T. Figure 5(d) shows the temperature dependence of R_H for $SnSe_2$. The negative Hall coefficient of $SnSe_2$ implies that $SnSe_2$ has electrons as major charge carriers, which is consistent with thermopower data. The variation of the carrier concentration with temperature is shown in Fig. 5(d). At room temperature, the carrier concentration of $SnSe_2$ is estimated to be 1.16×10^{18} cm^{-3}, consistent with the previous result [18]. With decreasing temperature, n_H decreases until 50 K. The upturn of n_H at lower temperatures is unexpected in the framework of thermally activated electrical conduction for both SnSe and $SnSe_2$. Further investigation is necessary to see if the drop of R_H is the consequence of mixed electrons and holes or magnetic-field-induced change in the electronic structure.

The Hall mobility of carriers can be calculated using $\mu_H = R_H\sigma$ [22]. Figures 5(e) and 5(f) present the temperature dependence of the Hall mobility of carriers for SnSe and $SnSe_2$ single crystals, respectively. At room temperature, μ_H ~ 400 cm^2 V^{-1} s^{-1} from σ_b and ~380 cm^2 V^{-1} s^{-1} from σ_c for SnSe and ~14 cm^2 V^{-1} s^{-1} for $SnSe_2$. The former is ~30 times higher than the latter. While it decreases with increasing temperature, μ_H for SnSe exhibits $1/T$ behavior, while μ_H for $SnSe_2$ follows $T^{-3/2}$ temperature dependence between 100 and 300 K, as represented by the solid lines in Figs. 5(e) and 5(f), respectively. The $1/T$ temperature dependence of μ_H reflects the dominant electron-phonon scattering in SnSe. The $T^{-3/2}$ temperature dependence of μ_H was also reported for

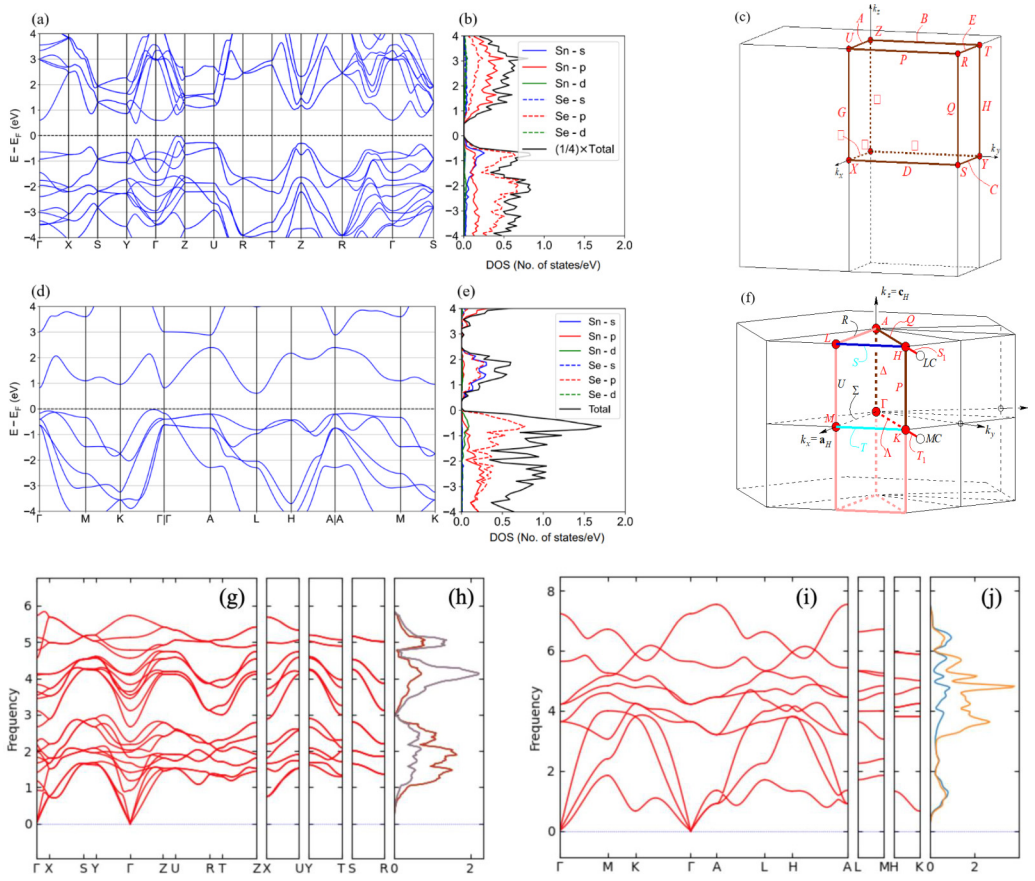

FIG. 6. (a) SnSe electronic structure, (b) density of states (DOS), and (c) Brillouin zone. (d) $SnSe_2$ electronic structure, (e) DOS, and (f) Brillouin zone. (g) SnSe phonon band structure and (h) partial DOS (PDOS) from Sn (gray) and Se (red). (i) $SnSe_2$ phonon band structure and (j) PDOS from Sn (blue) and Se (orange).

$SnSe_2$ between 300 and 700 K [18], which is attributed by electronic scattering by acoustic phonons at high temperatures. The carrier concentration increases nearly linearly with T for $SnSe_2$ [Fig. 5(d)], resulting in different temperature dependence of the electrical conductivity than that of SnSe.

To further shed insight on the studied systems, we calculate the structural, vibrational, and electronic properties of SnSe and $SnSe_2$. A Monkhorst-Pack $13\times13\times13$ $\vec{k}$-space integration mesh was used for the orthorhombic SnSe, while a Γ-centered $12\times12\times12$ $\vec{k}$-space integration grid was used for the hexagonal $SnSe_2$. A plane-wave basis energy cutoff of 720 eV and a Gaussian smearing of 0.05 eV yielded converged total energy and forces. The harmonic phonons were determined by using the PHONOPY code [48] with an atomic displacement value of 0.03 Å. A $2\times2\times2$ supercell was constructed to ensure convergence of the forces. VASP was used to compute the forces with an electronic energy convergence threshold of 10^{-8} eV using the same $\vec{k}$-space meshes that were used for determining the electronic and structural parameters. To calculate phonon spectra, 201 $\vec{k}$ points were used along each of the phonon band directions. For the partial DOS (PDOS), the same $\vec{k}$-space integration mesh used for the electronic structure calculations was also used. We obtain excellent structural parameters compared with our experimental results for both SnSe and $SnSe_2$. For hexagonal $SnSe_2$, the differences are 0.56% for a and 0.28% for c. For orthorhombic SnSe, the differences between our calculated and experimentally determined lattice parameters are 1.2% for a, 0.73% for b, and 0.77% for c. Compared with earlier calculations [6,49,50], our approach results in optimal lattice constants that are closest to experiment data. This implies the importance of considering vdW interaction, as the systems contain Se-Se bonds.

Figures 6(a) and 6(b) show the electronic structure and DOS of SnSe and $SnSe_2$, respectively. As it forms pyramidal structures connected by a single Se atom in the bc plane [see Fig. 1(c)], its bond length is ∼3% shorter than the other SnSe bond lengths (2.73 Å vs 2.82 Å). The pyramidal structures are separated by ∼2.94 Å along the a axis. As mentioned above, the vdW interaction between layers should be considered in simulation. Bader charge analysis yields a Sn site of 13.17 and 6.83 for Se, demonstrating a charge transfer from Sn to Se due to the larger Se electronegativity. The SnSe band structure indicates that SnSe is a semiconductor with an indirect band gap equal to 0.49 eV along the Γ-Z direction [see Fig. 6(c)]. This is higher than the experimentally obtained activation gap value, likely due to the band edge which is near E_f [Fig. 6(b)], which offers a conduction channel. This leads to underestimation of the energy gap through the measured electrical conductivity. The two-dimensional (2D) nature of

the SnSe bands can be seen by noticing how flat the bands along the Γ-X, S-Y, and Z-U directions. The band along R-T is also along this direction but is the highest occupied band <1 eV with the topmost one being flat. The bands along Γ-Y and Γ-Z have quite a bit of hybridization of Se-p_x, Sn-s, and Sn-p_x dominating over a wide energy range, which allows for more electron hopping. This indicates charge transfer from Sn to Se with the Sn losing almost 1 electron. This loss leaves Sn with $5p^1$, which is basically a filled band that stabilizes this Sn state below the Fermi energy, leaving the bands near E_f with mainly Se-p_x character. From Figs. 6(d) and 6(e), one can see that $SnSe_2$ is a semiconductor that has an indirect band gap equal to 0.63 eV and is again greater than the estimated activation gap from experiment. The latter is underestimated due to the edge states [Fig. 6(e)]. The 2D nature of the $SnSe_2$ bands can be realized by noticing how flat the bands are along the Γ-A (along the c axis) direction with the in-plane directions displaying more dispersion Γ-M, Γ-K, M-K, or L-H [see Fig. 6(f)]. Like SnSe, $SnSe_2$ is dominated by Se-p, Sn-s, and Sn-p bands near E_f. Due to the octahedral coordination, Sn has a larger charge transfer to Se than that in SnSe. Because there are 6 Se atoms (vs 3 in SnSe), there is slightly less charge transfer per Se atom in $SnSe_2$ (6.62 vs 6.83 for SnSe). Since $SnSe_2$ forms well-connected $SnSe_6$ octahedra that are separated by 2.96 Å with a Sn-Se bond length of 2.73 Å, the symmetry of this structure produces fewer bands near E_f than SnSe. The lower symmetry of the SnSe lattice produces more bands near E_f. This combined with the molecular nature of the subunits allows for hopping in SnSe via the Se atom that connects two units in an otherwise closed shell subunit. Such a difference results in better electrical conduction in SnSe than that of $SnSe_2$, as observed experimentally [Figs. 2(a) and 2(b)].

In addition, Figs. 6(b) and 6(e) show that there is a sharp decrease of DOS near E_f for both SnSe and $SnSe_2$. As mentioned previously, the large slope of DOS with respect to the energy $\frac{dN(E)}{dE}$ results in high thermopower, as presented in Fig. 3. Note that the slope for SnSe [plotted in Fig. 6(b) is $\frac{1}{4}$ of the total DOS] is larger than that for $SnSe_2$, consistent with the experimental data as well.

To understand the thermal transport properties, we have performed phonon calculations for the bands, PDOS, and the group velocities. Since we are interested in the low-lying acoustic modes, the simulations do not include nonanalytical terms that are modeled using the Born effective charge and macroscopic dielectric tensors necessary for accurate representation of longitudinal and transverse optical (LO-TO) modes splitting. The phonon band structure and PDOS for SnSe and $SnSe_2$ are shown in Figs. 6(g), 6(h) and 6(i), 6(j) including the band connections (decompositions of the basic modes, acoustic, longitudinal, transverse, etc.), respectively. For SnSe, there are 8 atoms in the unit cell, leading to 24 normal vibrational modes and with the full representation at the Γ point with $\Gamma = 4A_g + 4B_u^1 + 4B_u^3 + 4B_g^2 + 2A_u + 2B_u^2 + 2B_g^1 + 2B_g^3$. For $SnSe_2$, there are only 3 atoms in the unit cell, producing 9 normal modes with a full representation at the Γ point written as $\Gamma = 4E_u + 2A_u^2 + 2E_g + A_g^1$.

For SnSe, phonon bands and PDOS [see Figs. 6(g) and 6(h)] between 0 and 3.6 THz from the Sn and Se phonons completely overlap one another due to the long-wavelength coherent vibrations for acoustic phonons. The maximum and average group velocities of SnSe along high-symmetry directions from the Γ point are 37.176 and 7.546 Å THz for Γ-X, 34.389 and 6.606 Å THz for Γ-Y, and 28.937 and 6.187 Å THz for Γ-Z. For $SnSe_2$, the phonon states between 0 and 3.6 THz [see Figs. 6(i) and 6(j)] are again from the Sn and Se phonons completely overlapping one another due to the long-wavelength character of the acoustic phonons. The maximum and average group velocities, respectively, for $SnSe_2$ are 25.720 and 6.52 Å THz for Γ-A, 44.290 and 10.216 Å THz for Γ-H, 44.860 and 9.083 Å THz for Γ-K, 43.596 and 9.820 Å THz for Γ-L, and 45.067 and 10.076 Å THz for Γ-M. Note that the maximum and average group velocities for $SnSe_2$ are much higher relative to that for SnSe. This is most likely due to (1) the less open space between the SnSe substructure along the a axis (2.94 Å) for SnSe than that of $SnSe_2$ (2.96 Å) and (2) inequivalent Sn-Se bonding lengths in SnSe creating anharmonicity, as reported previously [5,6,49,50]. Our calculated result explains the lower thermal conductivity of SnSe than that of $SnSe_2$ observed experimentally [Figs. 4(a) and 4(b)].

IV. CONCLUSIONS

Single crystals of SnSe and $SnSe_2$ were successfully synthesized by the modified Bridgman method. The thermoelectric properties of both SnSe and $SnSe_2$ single crystals were studied between 2 and 400 K, which is absent in the literature. Both SnSe and $SnSe_2$ show semiconducting behavior at low temperatures, consistent with the DFT calculations. Although the carrier concentration of $SnSe_2$ is higher than that of SnSe, the former has the lower electrical conductivity than the latter system because of the unique hopping path in SnSe. This is also supported by the higher Hall mobility of carriers in SnSe than $SnSe_2$.

Overall, SnSe exhibits higher electrical conductivity and thermopower but lower thermal conductivity than that of $SnSe_2$, making it a higher figure of merit than the latter. The low thermal conductivity in SnSe is related to its layered structure and inequivalent Sn-Se bonding lengths, leading to slow phonon group velocities. Although the figure of merit at low temperatures is by no means high with ZT (400 K) ∼ 0.14, the unique crystal structure with high mobility makes SnSe a promising material platform for improved thermoelectric performance via stimuli such as chemical doping or strain effect.

ACKNOWLEDGMENT

This paper was partially supported by the Department of Energy through Grant No. DE-SC0024501.

[1] C. Gayner and K. K. Kar, Recent advances in thermoelectric materials, Prog. Mater. Sci. **83**, 330 (2016).

[2] D. Li, Y. Gong, Y. Chen, J. Lin, Q. Khan, Y. Zhang, Y. Li, H. Zhang, and H. Xie, Recent progress of

two-dimensional thermoelectric materials, Nano-Micro Lett. **12**, 36 (2020).
[3] M. N. Hasan, H. Wahid, N. Nayan, and M. S. Mohamed Ali, Inorganic thermoelectric materials: A review, Int. J. Energy Res. **44**, 6170 (2020).
[4] J. Wei, L. Yang, Z. Ma, P. Song, M. Zhang, J. Ma, F. Yang, and X. Wang, Review of current high-*ZT* thermoelectric materials, J. Mater. Sci. **55**, 12642 (2020).
[5] C. W. Li, J. Hong, A. F. May, D. Bansal, S. Chi, T. Hong, G. Ehlers, and O. Delaire, Orbitally driven giant phonon anharmonicity in SnSe, Nat. Phys. **11**, 1063 (2015).
[6] J. Hong and O. Delaire, Phase transition and anharmonicity in SnSe, Mat. Today Phys. **10**, 100093 (2019).
[7] S. Lin, W. Li, Z. Chen, J. Shen, B. Ge, and Y. Pei, Tellurium as a high-performance elemental thermoelectric, Nat. Commun. **7**, 10287 (2016).
[8] G. Chen, M. S. Dresselhaus, G. Dresselhaus, J. P. Fleurial, and T. Caillat, Recent developments in thermoelectric materials, Inter. Mater. Rev. **48**, 45 (2003).
[9] T. Zhu, Y. Liu, C. Fu, J. P. Heremans, J. G. Snyder, and X. Zhao, Compromise and synergy in high-efficiency thermoelectric materials, Adv. Mater. **29**, 1605884 (2017).
[10] B. Poudel, Q. Hao, Y. Ma, Y. Lan, A. Minnich, B. Yu, X. Yan, D. Wang, A. Muto, D. Vashaee *et al.*, High-thermoelectric performance of nanostructured bismuth antimony telluride bulk alloys, Science **320**, 634 (2008).
[11] D. J. Singh, Theoretical and computational approaches for identifying and optimizing novel thermoelectric materials, in *Recent Trends in Thermoelectric Materials Research II*, Semiconductors and Semimetals, edited by T. M. Tritt (Academic Press, New York, 2001), Vol. 70, Chap. 5, p. 125.
[12] A. J. Minnich, M. S. Dresselhaus, Z. F. Ren, and G. Chen, Bulk nanostructured thermoelectric materials: Current research and future prospects, Energy Environ. Sci. **2**, 466 (2009).
[13] J. Xin, H. Wu, X. Liu, T. Zhu, G. Yu, and X. Zhao, Mg vacancy and dislocation strains as strong phonon scatterers in $Mg_2Si_{1-x}Sb_x$ thermoelectric materials, Nano Energy **34**, 428 (2017).
[14] Y. Xu, W. Li, C. Wang, J. Li, Z. Chen, S. Lin, Y. Chen, and Y. Pei, Performance optimization and single parabolic band behavior of thermoelectric MnTe, J. Mater. Chem. A **5**, 19143 (2017).
[15] T. Wei, G. Tan, C. F. Wu, C. Chang, L. D. Zhao, J. Li, G. J. Synder, and N. G. Kanatzidis, Thermoelectric transport properties of polycrystalline SnSe alloyed with PbSe, Appl. Phys. Lett. **110**, 053901 (2017).
[16] L. D. Zhao, S. H. Lo, Y. Zhang, H. Sun, G. Tan, C. Uher, C. Wolverton, V. P. Dravid, and M. G. Kanatzidis, Ultralow thermal conductivity and high thermoelectric figure of merit in SnSe crystals, Nature (London) **508**, 373 (2014).
[17] A. T. Pham, T. H. Vu, C. Cheng, T. L. Trinh, J. E. Lee, H. Ryu, C. Hwang, S. K. Mo, J. Kim, L. D. Zhao *et al.*, High-quality $SnSe_2$ single crystals: Electronic and thermoelectric properties, ACS Appl. Energy Mater. **3**, 10787 (2020).
[18] A. T. Pham, T. H. Vu, Q. V. Nguyen, M. T. Vu, J. H. Park, S. D. Park, and S. Cho, Br-doped *n*-type $SnSe_2$: Single-crystal growth and thermoelectric properties, ACS Appl. Energy Mater. **4**, 2908 (2021).
[19] M. Jin, Z. Chen, X. Tan, H. Shao, G. Liu, H. Hu, J. Xu, B. Yu, H. Shen, J. Xu *et al.*, Charge transport in thermoelectric SnSe single crystals, ACS Energy Lett. **3**, 689 (2018).
[20] Y. Xue, Q. Wang, Z. Gao, X. Qian, J. Wang, G. Yan, M. Chen, L. D. Zhao, S. Wang, and Z. Li, Constructing quasi-layered and self-hole doped SnSe oriented films to achieve excellent thermoelectric power factor and output power density, Sci. Bull. **68**, 2769 (2023).
[21] M. Jin, J. Jiang, R. Li, X. Wang, Y. Chen, Y. Chen, and J. Xu, Thermoelectric properties of pure SnSe single crystal prepared by a vapor deposition method, Cryst. Res. Technol. **54**, 1900032 (2019).
[22] S. Wang, S. Hui, K. Peng, T. P. Bailey, W. Liu, Y. Yan, X. Zhou, X. Tang, and C. Uher, Low temperature thermoelectric properties of *p*-type doped single-crystalline SnSe, Appl. Phys. Lett **112**, 142102 (2018).
[23] P. C. Wei, S. Bhattacharya, J. He, S. Neeleshwar, R. Podila, Y. Y. Chen, and A. M. Rao, The intrinsic thermal conductivity of SnSe, Nature (London) **539**, E1 (2016).
[24] M. Liu, J. Zhang, J. Xu, B. Hu, B. Liu, K. Sun, Y. Yang, J. Wang, and B. Du, Phase structure, phase transition and thermoelectric properties of pristine and Br doped $SnSe_2$, J. Solid State Chem. **289**, 121468 (2020).
[25] H. Ju, M. Kim, D. Park, and J. Kim, A strategy for low thermal conductivity and enhanced thermoelectric performance in SnSe: Porous $SnSe_{1-x}S_x$ nanosheets, Chem. Mater. **29**, 3228 (2017).
[26] D. Ibrahim, C. Semprimoschnig, A. Dauscher, and B. Lenoir, Reinvestigation of the thermal properties of single-crystalline SnSe, Appl. Phys. Lett. **110**, 032103 (2017).
[27] G. Kresse and J. Hafner, *Ab initio* molecular dynamics for liquid metals, Phys. Rev. B **47**, 558 (1993).
[28] G. Kresse and J. Hafner, *Ab initio* molecular-dynamics simulation of the liquid-metal-amorphous-semiconductor transition in germanium, Phys. Rev. B **49**, 14251 (1994).
[29] G. Kresse and J. Furthmüller, Efficient iterative schemes for *ab initio* total-energy calculations using a plane-wave basis set, Phys. Rev. B **54**, 11169 (1996).
[30] G. Kresse and D. Joubert, From ultrasoft pseudopotentials to the projector augmented-wave method, Phys. Rev. B **59**, 1758 (1999).
[31] P. E. Blöchl, Projector augmented-wave method, Phys. Rev. B **50**, 17953 (1994).
[32] J. P. Perdew, K. Burke, and M. Ernzerhof, Generalized gradient approximation made simple, Phys. Rev. Lett. **77**, 3865 (1996).
[33] S. Grimme, Semiempirical GGA-type density functional constructed with a long-range dispersion correction, J. Comput. Chem. **27**, 1787 (2006).
[34] S. Grimme, J. Antony, S. Ehrlich, and H. Krieg, A consistent and accurate *ab initio* parametrization of density functional dispersion correction (DFT-D) for the 94 elements H-Pu, J. Chem. Phys **132**, 154104 (2010).
[35] S. Grimme, S. Ehrlich, and L. Goerigk, Effect of the damping function in dispersion corrected density functional theory, J. Comput. Chem. **32**, 1456 (2011).
[36] A. Tkatchenko and M. Scheffler, Accurate molecular van der Waals interactions from ground-state electron density and free-atom reference data, Phys. Rev. Lett. **102**, 073005 (2009).
[37] V. G. Ruiz, W. Liu, and A. Tkatchenko, Density-functional theory with screened van der Waals interactions applied to

atomic and molecular adsorbates on close-packed and non-close-packed surfaces, Phys. Rev. B **93**, 035118 (2016).

[38] J. Klimeš, D. R. Bowler, and A. Michaelides, Chemical accuracy for the van der Waals density functional, J. Phys.: Condens. Matter **22**, 022201 (2010).

[39] J. Klimeš, D. R. Bowler, and A. Michaelides, Van der Waals density functionals applied to solids, Phys. Rev. B **83**, 195131 (2011).

[40] H. Peng, Z.-H. Yang, J. P. Perdew, and J. Sun, Versatile van der Waals density functional based on a meta-generalized gradient approximation, Phys. Rev. X **6**, 041005 (2016).

[41] J. Ning, M. Kothakonda, J. W. Furness, A. D. Kaplan, S. Ehlert, J. G. Brandenburg, J. P. Perdew, and J. Sun, Workhorse minimally empirical dispersion-corrected density functional with tests for weakly bound systems: r^2SCAN+ rVV10, Phys. Rev. B **106**, 075422 (2022).

[42] P. Wu, Y. Ishikawa, M. Hagihala, S. Lee, K. Peng, G. Wang, S. Torii, and T. Kamiyama, Crystal structure of high-performance thermoelectric materials by high resolution neutron powder diffraction, Physica B **551**, 64 (2018).

[43] C. Julien, M. Eddrief, I. Samaras, and M. Balkanski, Optical and electrical characterizations of SnSe, SnS_2 and $SnSe_2$ single crystals, Mater. Sci. Eng. B **15**, 70 (1992).

[44] G. Domingo, R. S. Itoga, and C. R. Kannewurf, Fundamental optical absorption in SnS_2 and $SnSe_2$, Phys. Rev. **143**, 536 (1966).

[45] Y. Ding, B. Xiao, G. Tang, and J. Hong, Transport properties and high thermopower of $SnSe_2$: A full *ab-initio* investigation, J. Phys. Chem. C **121**, 225 (2017).

[46] S. S. Das, Md. G. Rosul, and M. Zebarjadi, Optimization of the thermoelectric properties of $SnSe_2$ using first-principles calculations, J. Phys. Chem. C **127**, 6916 (2023).

[47] N. W. Ashcroft and N. D. Mermin, *Solid State Physics* (Saunders College Publishing, Philadelphia, 1976), p. 488.

[48] A. Togo and I. Tanaka, First principles phonon calculations in materials science, Scr. Mater. **108**, 1 (2015).

[49] R. Gao, X. Wang, Y. Kuang, and B. Huang, First-principles study of anisotropic thermoelectric transport properties of IV-VI semiconductor compounds SnSe and SnS, Phys. Rev. B **92**, 115202 (2015).

[50] J. M. Skelton, L. A. Burton, S. C. Parker, A. Walsh, C.-E. Kim, A. Soon, J. Buckeridge, A. A. Sokol, C. R. A. Catlow, A. Togo *et al.*, Anharmonicity in the high-temperature *Cmcm* phase of SnSe: Soft modes and three-phonon interactions, Phys. Rev. Lett. **117**, 075502 (2016).